Strotos, G., Aleksis, G., Gavaises, M., Nikas, K-S., Nikolopoulos, N. & Theodorakakos, A. (2011). Non-dimensionalisation parameters for predicting the cooling effectiveness of droplets impinging on moderate temperature solid surfaces. International Journal of Thermal Sciences, 50(5), pp. 698-711. doi: 10.1016/j.ijthermalsci.2010.11.021

Non-dimensionalisation parameters for predicting the cooling effectiveness of droplets impinging on moderate temperature solid surfaces

George Strotos[1,§] , George Aleksis[1] , Manolis Gavaises[2] , Konstantinos-Stephen Nikas[1] , Nikos Nikolopoulos[1] , Andreas Theodorakakos[3]

[1] Technological Education Institute of Piraeus, Mechanical Engineering Department, Fluid Mechanics Laboratory, 250 Thivon & P. Ralli str., Aegaleo, 12244, Greece

[2] City University London, School of Engineering and Mathematical Sciences

Northampton Square, EC1V 0HB, London, UK

[3] Fluid Research Co. 49 Laskareos Str, 11472, Athens, Greece

[§] Correspondence author email: gstrot76@gmail.com

Abstract

The conjugate problem of fluid flow and heat transfer during the impact of water droplets onto a heated surface is studied numerically using the Volume of Fluid (VOF) methodology; adaptive grid refinement is used for increased resolution at the droplet moving interface. The phenomenon is assumed to be 2D-axisymmetric and the wall temperature is moderated to prevent the onset of nucleate boiling. Parametric studies examine the effect of Weber number, droplet size, wall initial temperature and liquid thermal properties on the cooling process of the heated plate during the impaction period. The main variables describing the evolution of the phenomenon are non-dimensionalised with expressions arising from the transient conduction theory. It is proved that for all cases examined, these non-dimensional expressions can be grouped together for describing the hydrodynamic and thermal behavior in a similar manner. Additionally, semi-analytic expressions are derived, which, for a given range of variation, describe the spatial distribution and the temporal evolution of the temperature of the wall as well also the heat flux absorbed from the droplet, cooling effectiveness and mean droplet temperature.

Keywords: droplet, heated wall, VOF, transient conduction

1 Introduction

The interaction of a droplet impinging on a solid wall is an interesting phenomenon which can be realized in many technological fields, such as internal combustion engines, cooling systems, fire suppression devices, printing and painting processes and metallurgical application amongst others. Previous studies suggest that the most influential parameters affecting the evolution of the phenomenon are the Weber (We) and the Reynolds (Re) numbers, the liquid-solid wetting contact angle and the surface roughness, the ambient gas pressure and properties, while the temperature of the wall relative to droplet's boiling point plays also a major role. The latter complicates even more the physical phenomenon since various hydrodynamic regimes may prevail at different wall temperatures. A combination of the aforementioned parameters can lead to various modes of impact such as spreading, rebounding or splashing followed by droplet disintegration into satellite droplets. On the other hand, the increase of the substrate's temperature can lead to four different regimes, namely film evaporation, nucleate boiling, transition boiling and film boiling. A detailed description of these phenomena can be found in [1] among others.

Due to its physical and industrial importance, a large number of experimental and numerical studies have been performed in order to shed light into the mechanisms governing this phenomenon. One of the earliest experimental studies was reported in [2], followed later by [3-17]. In these studies a wide range of We numbers, surface temperatures, liquid materials and surface qualities have been examined. Important information from these studies include the determination of the boundaries characterizing the outcome of the impinging regime, the estimation of the droplet lifetime impinging on a heated wall, the clarification of the parameters affecting droplet splashing and the estimation of maximum droplet spreading on the wall, as a function of the above mentioned parameters.

On the other hand, it is challenging to predict by numerical methodologies the various regimes identified during droplet collision on a heated surface. Over the past decades various methodologies have been proposed. The Marker and Cell (MAC) methodology was used by [18, 19], the Lagrangian formulation has been adopted by [20-25], the Immersed Boundary

Method (IBM) in [26, 27] and the Level-Set (LS) methodology in [28]. One of the most challenging methodologies is the VOF methodology proposed initially in [29] and also implemented in the present numerical study. This methodology has been used by [13, 30-35], in which the spreading of the droplet onto the wall was examined. In [31-33], the solidification of the droplet was also modeled, while in [34, 35] the levitation of the droplet for high surface temperatures was predicted. The VOF methodology has been also used from authors group using the GFS code [36] to predict various cases such as the impingement of a droplet on a substrate or on a liquid film [37-39], the interaction of a droplet with a heated wall coupled with evaporation [40-42], the evaporation of suspended single-component and multi-component droplets in a convective gas environment [43, 44] and also for binary droplet collisions [45-47]. In these works an adaptive local grid refinement technique was used [48] reducing the computational cost without loss of accuracy, in contrast with other methodologies which use a fixed numerical grid.

The present paper is an extension of the work presented by the authors group in [42]; in this earlier work, the numerical code employed also here has been validated against the experimental data of [13]. Here, the collision dynamics of a droplet hitting a heated wall is examined by considering initially a reference case; then, the influence of four parameters is investigated in detail, quantifying their effect on the heat transfer to the droplet. The details for the numerical conditions examined are listed in section 4.1. The We and Re numbers selected, as well as the low wall temperature, ensure that there is no droplet splashing and thus, the 2-dimensional axisymmetric numerical approach adopted here is justifiable. It is found that although the variables of interest may exhibit large variations in dimensional units, when the proposed non-dimensionalisation parameters are adopted, all cases can be described by simple relationships and semi-analytical expressions for the given range of variation investigated.

In the following sections of the paper, a short description of the methodology used and some basic relationships from transient heat conduction theory are presented initially, followed by a detailed description of the main heat and flow characteristics of the examined cases. Focus is put to the maximum droplet spreading, the detailed description of the temperature of the wall at the upper solid surface and on the axis of symmetry, the quantification of the heat flux absorbed from the droplet and the quantification of the droplet temperature. The conclusions of the present work are summarized at the end.

2 Mathematical model

The VOF methodology has been used in this study coupled with the solution of the conduction heat transfer equation inside the heated wall. The physical properties of liquid and gas are assumed to be function of local temperature and vapor concentration. The adopted methodology has been described in detail in [42]. The effect of droplet evaporation is included as in [42], together with the species diffusion term in the energy equation, as shown in [43, 44]; both terms play a minor role, but for reasons of completeness are taken into consideration. In [42] a fixed grid was used for the solid region and an adaptive local refined grid was applied in the gas-liquid interface in order to enhance accuracy and achieve low computational cost. The main numerical improvement of the present paper relative to the work of the authors presented in [42], is the use of adaptive grid refinement both for the gas-liquid and the solid phases during the simulation process. The advantage of this methodology is that it reduces the computational cost for the same level of accuracy. Furthermore, the computational cells on liquid-solid interface are common; this allows for more precise resolution of the non-linear field equations at the interface without the need for employing approximate interpolation schemes considering the neighborhood cells. Preliminary tests have shown that the predictions presented in [42] are reproduced by the present model with the same numerical accuracy at reduced computational cost. In the present study, 5 levels of local grid refinement are employed since this was found sufficient for grid independent solution to be achieved. The grid size at the vicinity of the gas-liquid interface is approximately equal to $D_0/130$ and the total cells required for the two grids used varied from 5200 at the beginning of the simulation to 14000 at the time of maximum spreading; a uniform grid with high resolution as that at the droplet interface would require approximately 1.3 million cells. The dynamic change of the grid at three instances during droplet spreading is shown in Fig. 1 together with an illustration of boundary conditions adopted in the present investigation; for reasons of distinctness of this particular figure, a case with four levels of local grid refinement is shown here. The boundary conditions used are described in more detail in [42]. The boundary condition at the liquid-solid-gas interface is imposed by modifying locally the volume forces acting to the droplet, according to the methodology proposed in [49].

3 Heat transfer theory

According to the transient conduction heat transfer theory [50, 51], when two semi-infinite solids noted as A and B, being initially at different uniform temperatures T_A and T_B respectively, are placed in contact, then their common surface reaches the so-called contact temperature given from:

$$T_c = \frac{\gamma_A T_A + \gamma_B T_B}{\gamma_A + \gamma_B} \tag{1}$$

$$\gamma = \sqrt{k \rho c_p} \tag{2}$$

where the temperatures are expressed in the Kelvin scale. Although the phenomenon is transient, the contact temperature remains constant in time and depends on the thermal properties and the initial temperatures of the two materials involved. The term γ is a weighting factor called thermal effusivity (also described as thermal capacitance in [1]) and plays an important role since large values of the ratio $\gamma^* = \gamma_A/\gamma_B$, results in a near isothermal material A, i.e. its temperature change is negligible compared to the corresponding temperature variation for material B. Since semi-infinite solids are assumed, the phenomenon is one-dimensional and the one-dimensional temperature distribution along the z-axis (e.g. in solid A) is given from:

$$\frac{T(z,t) - T_c}{T_A - T_c} = \mathrm{erf}(\eta) \quad \text{or} \quad \frac{T(z,t) - T_A}{T_c - T_A} = 1 - \mathrm{erf}(\eta) = \mathrm{erfc}(\eta) \tag{3}$$

where erf is the error function and erfc is the complementary error function. The variable η is a dimensionless similarity variable, defined as:

$$\eta = \frac{z}{2\sqrt{a_A t}} \tag{4}$$

where t=0 corresponds to the instant of first contact. Finally, the heat flux transferred through the interface of the solids changes in time and it is given from:

$$q''(0,t) = \frac{k_A (T_c - T_A)}{\sqrt{\pi a_A t}} = \frac{k_B (T_B - T_c)}{\sqrt{\pi a_B t}} \tag{5}$$

Although the theoretic contact temperature has been calculated assuming idealized conditions between two solid plates (i.e. one-dimensional heat conduction with absence of convection, semi-infinite solids, perfect contact at their interface and step change of temperature at the point of contact at the time t=0), it has been also used to predict the contact temperature of an impinging droplet onto a solid with a finite thickness. The first who made this consideration was [52] and hereafter many others followed. For the 2-dimensional cases examined here, the following relationships will form the basis of our analysis:

$$T_{c,th} = \frac{\gamma_{liq} T_{dr\,0} + \gamma_{sol} T_{w0}}{\gamma_{liq} + \gamma_{sol}}, \quad \gamma_{liq} = \sqrt{k_{liq} \rho_{liq} c_{p,liq}}, \quad \gamma_{sol} = \sqrt{k_{sol} \rho_{sol} c_{p,sol}}, \quad \gamma^* = \frac{\gamma_{sol}}{\gamma_{liq}} \tag{6}$$

$$T_w^*(z,r,t) = \frac{T(z,r,t) - T_{w0}}{T_{c,th} - T_{w0}}, \quad T_{dr}^*(z,r,t) = \frac{T(z,r,t) - T_{dr\,0}}{T_{c,th} - T_{dr\,0}} \tag{7}$$

$$T_{w,th}^*(z,t) = \mathrm{erfc}(\eta_{sol}), \quad \eta_{sol} = \frac{z}{2\sqrt{a_{sol} t}} \tag{8}$$

$$q''_{c,th}(z=0,r,t) = \frac{k_{liq}\left(T_{c,th} - T_{dr\,0}\right)}{\sqrt{\pi a_{liq} t}} = \frac{k_{sol}\left(T_{w0} - T_{c,th}\right)}{\sqrt{\pi a_{sol} t}} \tag{9}$$

Equations (7) are the definitions of the dimensionless temperature of wall and droplet and will be used throughout this study. Equation (8) is the theoretic dimensionless temperature distribution inside the solid phase and equation (9) is the theoretic transient heat flux transferred through the upper solid surface (z=0).

4 Results and discussion

4.1 Cases examined

The thermal behavior of the interaction of a droplet with a heated wall is controlled by many parameters such as the droplet spreading onto the wall and its surface oscillations, the temperature difference between the droplet and the wall, the temperature of the wall relative to the liquid boiling point, the pressure and the thermal properties of the different materials involved. On the other hand, the spreading onto the wall which affects heat transfer depends

on the impact velocity, the droplet size and the liquid physical properties as well as the liquid-solid contact angle. The purpose of the present study is to examine qualitatively the most influential of the abovementioned parameters and to derive correlations that group together the rather scatter nature of the temporal and spatial values of the flow and heat transfer parameters. A «reference» case study has been chosen and numerical experiments have been performed changing one parameter each time, creating triplets of data which reveal the effect of We number (We=40, 50, 60), the effect of droplet diameter (D_0=1, 2, 3mm), the effect of initial solid surface temperature (T_{w0}=80, 100, 120^{o}C) and finally the effect of the solid thermal properties relevant to the liquid droplet's one (γ^*=2.56, 5.1, 10.2). In the aforementioned triplets, the middle case corresponds to the reference case which is presented in detail in Table 1 while all other examined cases are summarized in Table 2; in Table 2 blank cells denote that the missing value is equal to the one of the reference case, shown at the top row of the table, while the first column of Table 2 corresponds to the label used for each case in the figures presented (e.g the label «ref» corresponds to the reference case). In all cases examined the liquid droplet was water, initially at a temperature of 20^{o}C with an advancing contact angle of 110^o and a receding contact angle of 10^o, which are typical values for water droplets impinging on a stainless steel surface [13, 53]. Although contact angles depend on temperature, these were assumed to be constant for the range of temperatures changes induced from the droplet impingement. The properties of the solid plate was those of a stainless steel, expect of those with different ratio γ^* (see Table 1 and Table 2). The surrounding gas was air at 20^{o}C and pressure 1 bar, while a constant heat flux q_b'' is provided to the wall from its lower surface so as to keep the upper solid surface temperature constant; the latter is estimated by considering steady state conditions [51]. In the simulations performed, the droplet was initially located at a distance equal to $1.5D_0$ from the wall; preliminary numerical experiments have confirmed that this distance was sufficient enough for the flow field around the impinging droplet to be developed as if the droplet was travelling from further upstream.

One of the most influential parameters affecting the droplet collision on a heated wall is the temperature of the wall relative to the droplet's boiling point. The wall temperatures examined and the We and Re numbers selected ensure that no nucleate boiling takes place, even in the case of the highest temperature of T_{w0}=120^{o}C [13]; for all cases examined, the droplet remains in contact with the heated wall. Furthermore, the selected We and Re numbers ensure that no three-dimensional structures are formed, according to the criterion for

droplet break-up proposed in [7], i.e. $Oh \cdot Re^{1.25} < 57.7$ for all cases examined. That justifies the 2-D axisymmetric approach adopted here.

As it will be shown in the following sections, the temporal evolution and the spatial distribution of the controlling hydrodynamic and thermal quantities exhibit large differences in dimensional units. On the other hand, using appropriate dimensionless parameters, all these data collapse to curves with much shorted range of variation between cases. This can provide a basis for the prediction of a large number of cases for the range of parameters investigated in the present paper.

The variables examined will be presented in two forms: a dimensional and a non-dimensional one. Time is non-dimensionalised with D_0/U_0 as $t^*=tU_0/D_0$; the convection timescale (D_0/U_0) has been widely used in droplet impingement dynamics where a wide range of droplet diameters and impact velocities have been considered, for example, [13, 18-20, 24-27] among others. The magnitudes which are related with temperature and heat fluxes will be non-dimensionalised using the theoretic contact temperature $T_{c,th}$ (see equations (7) and (9)) and not the initial wall temperature T_{w0} which seems to be the rational choice. This has been found to give better results, especially for the cases in which different solid thermal properties were assumed. It can also provide a measure of the deviation from the transient heat transfer theory for semi-infinite solids. Time t=0 corresponds to the time of first contact between the droplet and the solid surface. Finally, in order to increase the readability of the figures, some of the cases are omitted from the presented plots. Typically, these include the curves corresponding to the cases with different We number since they evolve generally in a very similar manner as the reference case.

4.2 Droplet spreading

The temporal evolution of droplet spreading on the solid surface for all cases examined is shown in Fig. 2a and Fig. 2b in dimensional and non-dimensional units, respectively. As it can be seen, all cases exhibit similar behavior. Initially, the droplet spreads rather fast onto the solid wall, reaching a maximum deformation and later it recoils towards its centre. After the pass of the recoiling phase, a second expansion takes place with decreasing amplitude since the available kinetic energy is gradually lost due to viscous dissipation. Finally, the droplet stagnates although its shape oscillates until it becomes stand still. The frequency of

the oscillations of the droplet's surface is in the order of $\sqrt{16\sigma/(\pi^2\rho D^3)}$ as suggested in [2]. This result to different oscillating periods for the droplets examined due to the variable droplet size and variation of its thermo-physical properties as influenced by the droplet's heating rate.

The maximum dimensionless spreading increases with increasing We number and droplet size. The initial solid surface temperature, as well as the solid thermal properties doesn't seem to affect the droplet's maximum spreading since the same advancing contact angle was assumed for all cases examined (the effect of contact angle in maximum spreading is shown later in equation (10)). In fact, an increasing theoretic contact temperature results in a slight increase of the droplet's spreading, since surface tension force at the triple phase region (solid-liquid-gas) decreases and allows for higher maximum spreading.

The prediction of the maximum spreading of a droplet impinging onto a wall has been addressed in many previous works, for example [5, 54-56]. A simple and reliable formula is that described in [54]:

$$\xi_{max,th} = \frac{D_{c,max}}{D_0} = \sqrt{\frac{We + 12}{3(1-\cos\theta_{adv}) + 4We/\sqrt{Re}}} \tag{10}$$

In the same reference, it has been estimated that the droplet reaches its maximum spreading theoretically at a non-dimensional time equal to:

$$t^*_{max,th} = \frac{8}{3} \tag{11}$$

Remarkably, this time does not depend on other parameters such as Re or We numbers. The present numerical results agree quite well with equations (10) and (11) within an accuracy of 2% for the maximal droplet spreading and 10% for the corresponding dimensionless time. Thus, equations (10) and (11) can be considered accurate enough and thus, they will be used throughout the present study for the derivation of semi-analytic expressions.

In Fig. 3 results from the simulated flow field of the reference case are presented at selected time instances. On the left-hand-side of the pictures of Fig. 3, the dimensionless velocity magnitude along with the streamlines is presented, while on the right-hand-side the dimensionless pressure is shown. The definitions of these magnitudes are:

$$U^{*}=\frac{U}{U_0}\quad,\quad p^{*}=\frac{p-\left(p_{\infty}+\frac{4\sigma}{D_0}\right)}{\frac{1}{2}\rho_{liq}U_0^2} \tag{12}$$

In the dimensionless pressure's definition, the term inside the brackets is equal to the initial pressure inside the droplet; using this definition, all cases exhibit the same value range for the pressure field independently of the droplet size and impact velocity. At the initial time instants of impact a maximum dimensionless pressure approximately equal to $p^{*}\approx 8$, is built up locally at the point of droplet's initial contact with the solid substrate, while the mean volume-averaged dimensionless droplet pressure is approximately 0.6 for all cases examined. Later on, the pressure becomes almost uniform inside the droplet with a mean value of -0.06 (lower compared to the initial droplet pressure); local picks can be observed at the droplet's rim and the advancing points that have a relatively high local radius of curvature. Inside the droplet a gas bubble is entrapped (caused from the initial pressure rise in the gas layer) as it can be seen in the enlarged region at $t^{*}=0.347$; this has been also reported in [1, 5]. The approaching droplet squishes the gas layer existing beneath it; this induces locally high gas velocities having magnitude approximately equal to $5U_0$. The droplet expands in the radial direction and reaches its maximum spreading when its initial kinetic energy is lost due to surface tension forces and viscous dissipation. Still, a portion of liquid mass continues to flow outwards forming a recirculation zone at the droplet's rim ($t^{*}=2.4$). Rim thickening and formation of a neck can be observed at the region where the rim is connected with the liquid forming the lamella. At subsequent times, the droplet starts to recede and at time $t^{*}\approx 4.4$ the lamella breaks-up at the symmetry axis; then, a hole at the droplet centre is formed. Nevertheless, due to the velocity field induced within the liquid phase, the lamella joins again with the remaining liquid inducing at the same time the entrapment of a gas bubble. The volume of the first bubble identified at $t^{*}=0.347$ is equal to around $6\cdot10^{-4}V_0$, while the volume of the second bubble entrapped at $t^{*}\approx 7$ is equal to around $7.5\cdot10^{-4}V_0$. The greater volume of the second bubble may be attributed to the different mechanisms controlling these phenomena.

4.3 Temperature at upper solid surface

The temporal evolution of the temperature of the upper solid surface at the centre of impact (z=0, r=0) is presented in Fig. 4a,b. Instead of presenting absolute temperature values, it is

more convenient to present the temperature drop relative to the initial wall temperature, since various initial solid surface temperatures have been considered. The time axis is now dimensional (in ms), since as referred in [13], the temperature of the solid surface drops very fast, irrespectively of the impact velocity and droplet size; this is confirmed by the present analysis as well. The cooling of the substrate depends generally on the initial temperature of the droplet which is not examined here since a constant initial droplet temperature equal to T_{dr0}=20^{o}C for all cases examined has been considered. It also depends on the initial solid surface temperature T_{w0} and on the ratio of thermal properties of the liquid and solid phases, expressed by the variable γ^{*}. Surface cooling increases with increasing initial surface temperature since there is a greater amount of energy available to be transferred and decreases with an increase of the ratio γ^{*}. Other parameters, such as We number and droplet size doesn't affect the temperature drop; this is in accordance with the findings reported in [13]. In Fig. 4c the aforementioned plots are non-dimensionalised with the theoretic temperature drop i.e. $T_{c,th}$-T_{w0}; the experimental results of [8, 13] are also presented. For reasons of distinctness of these plots, only representative curves are shown. In [13] a water droplet at 25^{o}C falling onto a stainless steel solid surface initially at 120^{o}C was examined, while in [8] water and n-heptane droplets (γ_{water}=1589, $\gamma_{heptane}$=435) falling on stainless steel surface at 90 ^{o}C and 70 ^{o}C, respectively, were examined. As it can be seen, the present results are well compared with the experimental data of [8, 13]. It is interesting to notice that for all cases examined here, the solid surface temperature changes in a similar manner. The dimensionless temperature drop is fast, reaching values between 1.4 and 1.6. It is worth noticing that the wall temperature falls below the theoretic contact temperature; this fact is clearly shown in the experimental works of [8, 57, 58] and according to [8], the enhanced surface cooling is owed to the forced convective motion of the droplet. The wavy form of the curves is a result of the gas bubble entrapped, which affects the thermodynamic properties locally at this region and affects the temperature evolution. Furthermore, the movement of the gas bubble and not just its presence amplifies this phenomenon.

Continuing, the temporal evolution of the temperature of the upper surface of the solid at various distances from the axis of symmetry (z=0, r) is presented in Fig. 5; these results correspond to the reference case. The temperature at the axis of symmetry along with the predicted temperature history at r/R_{max}= 0.25, 0.5, 0.75, 1.00 and 1.25 are shown. There is a time delay for the response of the temperature as the distance from the axis of symmetry is increasing, as also a lower decrease in temperature. At r=1.25R_{max} the solid temperature is almost unaffected from the droplet collision (the dimensionless temperature is less than 0.03) and further analysis for all cases examined showed that a 5% dimensionless temperature drop

occurs at a distance between 1.15 and 1.25R_{max}. This is an important outcome since it is concluded that for an effective spray cooling, droplets should have a distance between them less than 1.3-1.5 of their maximum spreading.

4.4 Solid temperature at centre at various depths from the upper surface

Having examined the upper surface of the substrate, the temporal evolution of the solid temperature on the axis of symmetry (r=0) at various distances from the upper surface is studied. Three distances from the upper solid surface were considered located at z=0.1, 0.2 and 0.3mm, respectively. The results of all cases examined are shown in Fig. 6a, b and c respectively. The comments made for Fig. 4 also apply in this case. Additionally, the temperature inside the wall is less affected as the distance from the surface increases. Moreover, there is a slower response to the temperature change with increasing distance. Despite the fact that the curves in Fig. 6a, b and c exhibit a different behavior since they are both time and space dependent, they can be grouped together by non-dimensionalising the temperature in the same way as in Fig. 4c and the time by using the timescale $z^2/4\alpha_{sol}$ which arises from the similarity variable of equation (4). Now all curves exhibit a similar behavior; deviations are observed only during the recoiling phase (Fig. 6d) due to the different droplet oscillating frequency. It has to be noted that the non-dimensional temperature could be plotted versus the dimensionless similarity variable η which could also give promising results; however this case was not found convenient as this parameter is inversely proportional to time.

4.5 Plots at maximum spreading

After having examined the temporal evolution of the most influential parameters, our interest is now focusing on the spatial distribution of temperature at the characteristic time of maximum spreading ($t=t_{max}$). The temperature distribution relative to the initial solid surface temperature inside the solid wall in the symmetry axis versus the distance from the upper

surface is plotted in Fig. 7a. As it can be seen, there is a high temperature drop at the surface and as the distance from the upper surface increases, the temperature seems to be unaffected from the droplet collision. A general conclusion cannot be extracted from the curves in Fig. 7a. On the other hand, by non-dimensionalising the temperature and plotting it versus the dimensionless similarity variable of equation (8), all curves converge to a single one as shown in Fig. 7b. A satisfactory approximation of these curves, although not necessarily a best fit, is:

$$T_w^* = 1.4 \cdot \mathrm{erfc}\left(\frac{z}{2\sqrt{a_{sol} t}} \right) \qquad (13)$$

In this expression, the factor 1.4 denotes the deviation from the transient conduction heat transfer theory expressed by equation (8). The curve corresponding to equation (13) is also shown in Fig. 7b. This relation has greater validity since it depends both on the time and the depth inside the wall. An inspection of Fig. 6d and Fig. 7b reveals that equation (13) can be used to describe satisfactory the temperature of every point of the wall in the symmetry axis at any time.

Finally the distribution of temperature and heat flux in the radial direction on the upper solid surface (z=0, $t=t_{max}$) is studied. The temperature distribution is shown in Fig. 8a; Fig. 8b expresses the same variation but this time in dimensionless form. The radial distance is non-dimensionalised with the theoretic maximum contact radius. The dimensionless temperature distribution has the same form for all cases examined. Its wavy form is primarily owed to the non-uniform thickness of the liquid mass and secondarily to the non-perfect contact of the liquid phase with the wall, i.e. the entrapment of a small portion of gas between the liquid and the solid. The corresponding heat flux distribution is shown in Fig. 8c and Fig. 8d in dimensional and non-dimensional units, respectively, adopting equation (9). The reasons for selecting the transient reference heat flux are explained in section 4.6. The heat flux distribution has the same form for all cases examined and its maximum values are observed at the edge of the droplet, where the cold liquid front meets the hot wall. This is also governed by a wavy form and a local maximum is observed at $0.6\text{-}0.7R_{max}$ due to the neck formed at this region. Similar trends for the temperature and the heat flux distribution have been presented in previous numerical studies such as those of [13, 27].

In Fig. 9 the dimensionless temperature field $T^* = \left(T - T_{dr\,0}\right) / \left(T_{c,th} - T_{dr\,0}\right)$ is shown on right-hand-side and the corresponding heat flux field on the left-hand-side, respectively. The heat flux is non-dimensionalised with equation (9), i.e. $q^* = q'' / q''_{c,th}(t)$; the discontinuity shown on the plots at the area of common faces of solid and liquid-gas region is not real but arises

from a limitation of the graphics software used to calculate the gradients of temperature when connecting grids are used. The temperature beneath the liquid falls rapidly in the entire contact region during the droplet expansion. At the receding phase, despite the fact that the droplet has reduced its contact region with the wall, the wall's temperature remains still low (t^*=7.188) at the points where there was a previous contact. The gas phase temperature exhibits a spatial distribution affected by the recirculation zone in the gas phase (see Fig. 3).The dimensionless heat flux exhibits its pick values at the front of the droplet and at the points where the lamella is thinner.

4.6 Mean heat flux per unit area absorbed from the droplet

The time evolution of the mean heat flux per unit area absorbed by the droplet is shown in Fig. 10a. The heat flux transferred to the liquid droplet exhibits large values at the initial stages of contact (theoretically infinity) and then decreases with time more than one order of magnitude. It increases with increasing theoretical contact temperature and with decreasing droplet size.

In [13] the mean heat flux absorbed by the droplet was estimated using the boundary layer theory for axisymmetric stagnation flow. Preliminary tests performed here confirm the formula proposed in [13] but with the replacement of T_{w0} with $T_{c,th}$; this can provide a good non-dimensionalisation for the curves of Fig. 10a since they all converge to a single one and at time of maximum spreading they all have a value equal to around 1.4. On the other hand, the problem that they all change more than one order of magnitude during the evolution of the spreading still exists.

The approach adopted here, is to non-dimensionalise the curves of Fig. 10a with the transient conduction heat flux of equation (9) expressed from the liquid side. The results are shown in Fig. 10b and as seen, all curves are grouped together and furthermore, the temporal variation of dimensionless heat flux has been suppressed (it varies between 1 and 2 due to the oscillatory motion of droplet on the wall); thus it can be considered relatively constant in time and equal to 1.7. This is an important outcome, since the mean heat flux absorbed from the droplet can be estimated as:

$$q''_{liq,mean}(t) \approx 1.7 \cdot q''_{c,th}(t) = 1.7 \cdot \frac{k_{liq}\left(T_{c,th} - T_{dr\,0}\right)}{\sqrt{\pi a_{liq} t}} \qquad (14)$$

4.7 Thermal energy absorbed from the droplet

The total energy absorbed by the droplet is also of interest to a number of applications. This can be estimated through integration of the heat flux absorbed from the droplet in time and space. The results are shown in Fig. 11a. The energy absorption from the droplet increases with droplet size and impact velocity, since the available area for the heat to be transferred increases as also increases with the increase of the theoretical contact temperature. The cooling effectiveness of the droplet was defined in [13] as the energy absorbed from the droplet, non-dimensionalised with the maximum energy that the droplet can absorb, while the phase change was neglected since it plays a minor role for the low wall temperatures examined. Here a similar approach is adopted, but the initial wall temperature T_{w0} has been replaced with the theoretic contact temperature $T_{c,th}$:

$$\varepsilon(t) = \frac{Q_{liq,tot}}{Q_{liq,maximum}} = \frac{\int_0^t \left(\int_0^A q''_{liq} \, dA \right) dt}{m_{liq} c_{p,liq} \left(T_{c,th} - T_{dr\,0} \right)} \qquad (15)$$

This parameter is plotted versus the non-dimensional time in Fig. 11b. It is increased for small droplets due to their smaller thermal mass and high We numbers due to increased spreading, while the theoretic contact temperature doesn't affect significantly the cooling effectiveness.

For practical applications, it may be of interest to predict in an analytic way the cooling effectiveness without the need of solving the complicated field equations. A semi-analytical expression for the temporal evolution of cooling effectiveness can be obtained by combining equation (15) with the transient conduction heat flux of equation (14) and integrate in time and space:

$$\varepsilon_{th}(t) = 1.7 \cdot \frac{3\sqrt{a_{liq}}}{2\sqrt{\pi} D_0} \int_0^t \frac{\xi^2}{\sqrt{t}} dt \qquad (16)$$

The correction factor of 1.7 has been used to correct the heat flux as it has been shown in previous section 4.6. In the integral of the nominator of equation (16), a transformation of t into t^* can be performed:

$$\varepsilon_{th}(t) = 1.7 \cdot \frac{3}{2\sqrt{\pi}} \frac{1}{\sqrt{\mathrm{Re}\,\mathrm{Pr}}} \int_0^{t^*} \frac{\xi^2}{\sqrt{t^*}} dt^* \qquad (17)$$

Also, the following definitions are adopted:

$$\omega\left(t^*\right) = \frac{\xi^2}{\sqrt{t^*}}, \quad \Omega(t^*) = \int_0^{t^*} \omega dt^* \qquad (18)$$

Based on the definitions (18), the theoretic cooling effectiveness is given from:

$$\varepsilon_{th}(t) = 1.7 \cdot \frac{3}{2\sqrt{\pi}} \frac{1}{\sqrt{\mathrm{Re}\,\mathrm{Pr}}} \Omega(t^*) \qquad (19)$$

The integral Ω is difficult to be calculated analytically and in Appendix it is estimated by using numerical integration as:

$$\Omega(t^*) \approx \omega_{max,th} \cdot f_{fit}(t^*) \qquad (20)$$

$$\omega_{max,th} = \omega\left(t^*_{max,th}\right) = \frac{\xi^2_{max,th}}{\sqrt{t^*_{max,th}}} \qquad (21)$$

$$f_{fit}(t^*) = 7.55422 \cdot \mathrm{EXP}\left(-\frac{2.93638}{t^* + 0.29491}\right) \qquad (22)$$

where the subscript «max» refers to the time of maximum spreading. Finally, the semi-analytical expression for the cooling effectiveness is:

$$\varepsilon_{th}(t) = 1.7 \cdot E_{max,th} \cdot f_{fit}(t^*) \qquad (23)$$

$$E_{max,th} = \frac{3}{2\sqrt{\pi}} \frac{1}{\sqrt{\mathrm{Re}\,\mathrm{Pr}}} \omega_{max,th} \qquad (24)$$

In Fig. 12a the cooling effectiveness predicted with the VOF methodology is plotted normalized with the term $E_{max,th}$, while the theoretical fit curve is also shown. The semi-analytical expression predicts accurately the normalized cooling effectiveness of droplets. Small deviations exist at the receding phase due to the different recoiling frequencies of the droplets. This is an important outcome, since an expression can now been given to quantify the thermal energy absorbed from the droplet at any time:

$$Q_{liq,tot}(t^*) = Q_{liq,maximum} \cdot E_{max,th} \cdot 1.7 \cdot f_{fit}(t^*) \qquad (25)$$

Randomly selected cases of Fig. 11a are re-plotted in Fig. 12b along with curves corresponding to the semi-analytical expression of equation (25) denoted with symbols. The discrepancies observed at the recoiling phase could be avoided if a more accurate expression for the integral Ω (e.g. a fit curve of a tenth degree polynomial) and for the assumed value of the heat flux absorbed from the droplet of equation (14), i.e. a sinusoidal function, were used. On the other hand, such a calculation is not performed here since the aim of the present analysis is to keep it as simple as possible.

4.8 Mean droplet temperature

Droplets during their impact and spreading on the hotter surface are heated-up. The temporal evolution of the mean volume-averaged droplet temperature for all cases examined is shown in Fig. 13a. Initially the droplet's temperature increases rapidly and later it continues to increase but with a decreasing rate. The heating rate of the droplet is mainly affected by the temperature difference between the droplet and the substrate, which decreases with time and results in a decreasing droplet's heating rate. Droplet's warming-up increases with the increase of the theoretic contact temperature, with increasing We number since there is more available contact area for heat transfer and finally increases with decreasing droplet size owed to the decrease of the available thermal mass ($\sim \rho D^3 c_p$). On the other hand, evaporation source terms tend to suppress the temperature rise, but this effect is less important for the conditions considered here. The non-dimensional temperature increase of the droplet using the theoretic contact temperature is shown in Fig. 13b.

It is interesting to examine theoretically the temperature of the droplet. An energy balance on the droplet's mass gives:

$$\rho_{liq} V c_{p,liq} \frac{\partial T}{\partial t} = q''_{liq} A_c \quad , V = \frac{\pi D_0^3}{6}, \qquad A_c = \frac{\pi D_c^2}{4} \tag{26}$$

Using the transient heat flux of equation (14), the dimensionless heating rate of the droplet is equal to:

$$\frac{\partial T^*_{dr}}{\partial t^*} = E_{th} = \frac{3}{2\sqrt{\pi}} \frac{1}{\sqrt{Re\,Pr}} \frac{\xi^2}{\sqrt{t^*}} \tag{27}$$

where E_{th} represents the dimensionless temperature change rate (the same magnitude expressed at maximum spreading has also been appeared in section 4.7). By integrating equation (27) in time, it can be concluded that the temporal evolution of the dimensionless mean droplet temperature is given from the same relationship as the one of the cooling effectiveness:

$$T^{*}_{dr,mean} \equiv \varepsilon_{th} = E_{max,th} \cdot 1.7 \cdot f_{fit}(t^{*}) \qquad (28)$$

The latter is not surprising, since the nominator and the denominator of equation (15) represent the right and the left-hand-side, respectively, of equation (26) when integrated in time; that is why Fig. 11b is identical to Fig. 13b. Unfortunately, the aforementioned results have not yet been validated against experimental data; the only relevant published work is that [15], but the results presented there refer to the total temperature rise of droplets and not the temporal evolution of the temperature, which bounce off a heated wall. Furthermore, the wall temperatures examined in [15] are close to the Leidenfrost point; thus, direct comparison with the present results cannot be performed.

5 Conclusions

The VOF methodology has been used to predict the complicated transport phenomena occurring during the impact of a droplet onto a heated wall at the film evaporation regime, while an adaptive local grid refinement technique was used in both the liquid-gas and liquid-solid regions, achieving low computational cost without loss of accuracy. The effect of We number, droplet size, wall temperature and solid thermal properties has been studied parametrically. Using appropriate non-dimensionalisation variables which originate from the transient heat conduction theory for semi-infinite solids, it has been proved that a wide range of cases can be described by simple semi-analytical expressions. If the theoretic contact temperature, maximum theoretic spreading and the corresponding time are known from the equation (6) , (10) and (11), respectively, then the following conclusions can be drawn:

1) The dimensionless temperature of the upper solid surface at the symmetry axis falls 40-60% more than theoretically expected one, while it is almost unaffected at $1.25R_{max}$ in the radial direction.

2) The in-depth dimensionless temperature of the wall at the symmetry axis can be given by equation (13). A 40% deviation from the transient conduction heat transfer theory exists.

3) The heat flux absorbed from the droplet exhibits large variations in time and it is approximately 70% higher than the theoretic one given by equation (14).

4) The temporal evolution of the cooling effectiveness of a droplet and its dimensionless temperature are described from the same semi-analytic expression, i.e. equation (28) along with equations (21),(22) and (24).

6 Appendix

In the analysis in section 4.7 the term $\omega\left(t^*\right)=\xi^2/\sqrt{t^*}$ and the integral Ω appear. The integral Ω is difficult to be calculated analytically, since an analytic expression for the temporal evolution of dimensionless spreading does not exist. In order to calculate its value, the term ω is plotted in Fig. 14a normalized with its value calculated theoretically at maximum spreading $\omega_{max,th}=\omega\left(t^*_{max,th}\right)$ for all cases simulated and integrated numerically as shown in Fig. 14b. A best fit curve for the data of Fig. 14b is used to approximate the integral Ω. This curve, called f_{fit}, is also shown in Fig. 14b and it is given from the relationship:

$$\Omega(t^*)\approx\omega_{max,th}\cdot f_{fit}(t^*) \quad , \quad \omega_{max,th}=\omega\left(t^*_{max,th}\right)=\frac{\xi^2_{max,th}}{\sqrt{t^*_{max,th}}}$$

$$f_{fit}(t^*)=7.55422\cdot EXP\left(-\frac{2.93638}{t^*+0.29491}\right)$$

7 Nomenclature

Roman symbols

Symbol	Description	Units
A	surface area	m^2
c_p	heat capacity	J/kgK
D	droplet diameter	m
E_{th}	theoretic non-dimensional droplet temperature change rate	-
k	thermal conductivity	W/mK
Oh	Ohnesorge number $Oh = \mu_{liq} / \sqrt{\rho_{liq} \sigma D_0}$	-
p	pressure	Pa
Pr	Prandtl number	-
q	heat transfer rate	W
q''	heat flux	W/m^2
q''_b	heat flux given from below	W/m^2
Q	thermal energy	J
R	radius	m
r	distance from symmetry axis	m
Re	Reynolds number $Re = \rho_{liq} U_0 D_0 / \mu_{liq}$	-
T	temperature	K
t	time	s
$T_{c,th}$	theoretic contact temperature of semi-	K

	infinite solids	
U	velocity	m/s
V	volume	m^3
We	Weber number $We = \rho_{liq} U_0^2 D_0 / \sigma$	-
z	distance from upper surface	m

Greek symbols

Symbol	Description	Units
α	thermal diffusivity	m^2/s
γ	thermal effusivity	$J/m^2Ks^{0.5}$
γ^*	ratio of thermal effusivities $\gamma_{sol}/\gamma_{liq}$	-
ε	cooling effectiveness	-
η	similarity variable	-
θ	contact angle	degrees
μ	viscocity	kg/ms
ξ	spread factor	-
ρ	density	kg/m^3
σ	surface tension	N/m
Φ	general magnitude	
ω	term $\xi^2 / \sqrt{t^*}$	-
Ω	integral of $\omega / \omega_{max,th}$	-

Subscripts

Symbol	Description
0	initial
∞	infinity
adv	advancing
c	contact
dr	droplet
liq	liquid
max	at maximum spreading
rec	receding
sol	solid
th	theoretic value
w	wall

Overscripts

Symbol	Description
Φ^*	non-dimensional Φ
Φ''	Φ per unit area

8 References

[1] Rein M., Drop-Surface Interactions, Springer, New York, 2002.

[2] Wachters L.H.J., Westerling N.A., The Heat transfer from a hot wall to impinging water drops in the spheroidal State, Chem. Eng. Science, 21 (1966) 1047-1056.

[3] Akao F., Araki K., Mori S., Moriyama A., Deformation behaviors of a liquid droplet impinging onto hot metal surface, Transactions of the Iron and Steel Institute of Japan, 20 (1980) 737-743.

[4] Xiong T.Y., Yuen M.C., Evaporation of a Liquid Droplet on a Hot Plate, International Journal of Heat and Mass Transfer, 34 (1991) 1881-1894.

[5] Chandra S., Avedisian C.T., On the Collision of a Droplet with a Solid-Surface, Proceedings of the Royal Society of London Series a-Mathematical Physical and Engineering Sciences, 432 (1991) 13-41.

[6] Anders K., Roth N., Frohn A., The Velocity Change of Ethanol Droplets During Collision with a Wall Analyzed by Image-Processing, Experiments in Fluids, 15 (1993) 91-96.

[7] Mundo C., Sommerfeld M., Tropea C., Droplet-wall collisions: experimental studies of the deformation and breakup process, International Journal of Multiphase Flow, 21 (1995) 151-173.

[8] Qiao Y.M., Chandra S., Boiling of droplets on a hot surface in low gravity, International Journal of Heat and Mass Transfer, 39 (1996) 1379-1393.

[9] Ko Y.S., Chung S.H., An experiment on the breakup of impinging droplets on a hot surface, Experiments in Fluids, 21 (1996) 118-123.

[10] Bernardin J.D., Mudawar I., Walsh C.B., Franses E.I., Contact angle temperature dependence for water droplets on practical aluminum surfaces, International Journal of Heat and Mass Transfer, 40 (1997) 1017-1033.

[11] Bernardin J.D., Stebbins C.J., Mudawar I., Mapping of impact and heat transfer regimes of water drops impinging on a polished surface, International Journal of Heat and Mass Transfer, 40 (1997) 247-267.

[12] Bernardin J.D., Stebbins C.J., Mudawar I., Effects of surface roughness on water droplet impact history and heat transfer regimes, International Journal of Heat and Mass Transfer, 40 (1997) 73-88.

[13] Pasandideh-Fard M., Aziz S.D., Chandra S., Mostaghimi J., Cooling effectiveness of a water drop impinging on a hot surface, International Journal of Heat and Fluid Flow, 22 (2001) 201-210.

[14] Sikalo S., Marengo M., Tropea C., Ganic E.N., Analysis of impact of droplets on horizontal surfaces, Experimental Thermal and Fluid Science, 25 (2002) 503-510.

[15] Castanet G., Lienart T., Lemoine F., Dynamics and temperature of droplets impacting onto a heated wall, International Journal of Heat and Mass Transfer, 52 (2009) 670-679.

[16] Shen J., Graber C., Liburdy J., Pence D., Narayanan V., Simultaneous droplet impingement dynamics and heat transfer on nano-structured surfaces, Experimental Thermal and Fluid Science, 34 (2009) 496-503.

[17] Panao M.R.O., Moreira A.L.N., Heat transfer correlation for intermittent spray impingement: A dynamic approach, International Journal of Thermal Sciences, 48 (2009) 1853-1862.

[18] Hatta N., Fujimoto H., Takuda H., Deformation process of a water droplet impinging on a solid surface, Journal of Fluids Engineering, Transactions of the ASME, 117 (1995) 394-401.

[19] Fujimoto H., Hatta N., Deformation and rebounding processes of a water droplet impinging on a flat surface above leidenfrost temperature, Journal of Fluids Engineering-Transactions of the ASME, 118 (1996) 142-149.

[20] Zhao Z., Poulikakos D., Fukai J., Heat transfer and fluid dynamics during the collision of a liquid droplet on a substrate .1. Modeling, International Journal of Heat and Mass Transfer, 39 (1996) 2771-2789.

[21] Fukai J., Shiiba Y., Miyatake O., Theoretical study of droplet impingement on a solid surface below the Leidenfrost temperature, International Journal of Heat and Mass Transfer, 40 (1997) 2490-2492.

[22] Waldvogel J.M., Poulikakos D., Solidification phenomena in picoliter size solder droplet deposition on a composite substrate, International Journal of Heat and Mass Transfer, 40 (1997) 295-309.

[23] Butty V., Poulikakos D., Giannakouros J., Three-dimensional presolidification heat transfer and fluid dynamics in molten microdroplet deposition, International Journal of Heat and Fluid Flow, 23 (2002) 232-241.

[24] Bhardwaj R., Longtin J.P., Attinger D., A numerical investigation on the influence of liquid properties and interfacial heat transfer during microdroplet deposition onto a glass substrate, International Journal of Heat and Mass Transfer, 50 (2007) 2912-2923.

[25] Bhardwaj R., Attinger D., Non-isothermal wetting during impact of millimeter-size water drop on a flat substrate: Numerical investigation and comparison with high-speed visualization experiments, International Journal of Heat and Fluid Flow, 29 (2008) 1422-1435.

[26] Francois M., Shyy W., Computations of drop dynamics with the immersed boundary method, Part 1: Numerical algorithm and buoyancy-induced effect, Numerical Heat Transfer, Part B: Fundamentals, 44 (2003) 101-118.

[27] Francois M., Shyy W., Computations of drop dynamics with the immersed boundary method, Part 2: Drop impact and heat transfer, Numerical Heat Transfer, Part B: Fundamentals, 44 (2003) 119-143.

[28] Ge Y., Fan L.S., 3-D Direct Numerical Simulation of Gas-Liquid and Gas-Liquid-Solid Flow Systems Using the Level-Set and Immersed-Boundary Methods, in: Advances in Chemical Engineering, 2006, pp. 1-63.

[29] Hirt C.W., Nichols B.D., Volume of Fluid (Vof) Method for the Dynamics of Free Boundaries, Journal of Computational Physics, 39 (1981) 201-225.

[30] Trapaga G., Szekely J., Mathematical modeling of the isothermal impingement of liquid droplets in spraying processes, Metallurgical transactions. B, Process metallurgy, 22 (1991) 901-914.

[31] Liu H., Lavernia E.J., Rangel R.H., Numerical simulation of substrate impact and freezing of droplets in plasma spray processes, Journal of Physics D: Applied Physics, 26 (1993) 1900-1908.

[32] Pasandideh-Fard M., Bhola R., Chandra S., Mostaghimi J., Deposition of tin droplets on a steel plate: simulations and experiments, International Journal of Heat and Mass Transfer, 41 (1998) 2929-2945.

[33] Bussmann M., Mostaghimi J., Chandra S., On a three-dimensional volume tracking model of droplet impact, Physics of Fluids, 11 (1999) 1406-1417.

[34] Harvie D.J.E., Fletcher D.F., A hydrodynamic and thermodynamic simulation of droplet impacts on hot surfaces, Part I: theoretical model, International Journal of Heat and Mass Transfer, 44 (2001) 2633-2642.

[35] Harvie D.J.E., Fletcher D.F., A hydrodynamic and thermodynamic simulation of droplet impacts on hot surfaces, Part II: validation and applications, International Journal of Heat and Mass Transfer, 44 (2001) 2643-2659.

[36] Fluid_Research_Company, Manual on the GFS CFD code, in, 2002 , www.fluid-research.com.

[37] Nikolopoulos N., Theodorakakos A., Bergeles G., Normal impingement of a droplet onto a wall film: a numerical investigation, International Journal of Heat and Fluid Flow, 26 (2005) 119-132.

[38] Theodorakakos A., Ous T., Gavaises A., Nouri J.M., Nikolopoulos N., Yanagihara H., Dynamics of water droplets detached from porous surfaces of relevance to PEM fuel cells, Journal of Colloid and Interface Science, 300 (2006) 673-687.

[39] Nikolopoulos N., Theodorakakos A., Bergeles G., Three-dimensional numerical investigation of a droplet impinging normally onto a wall film, Journal of Computational Physics, 225 (2007) 322-341.

[40] Nikolopoulos N., Theodorakakos A., Bergeles G., A numerical investigation of the evaporation process of a liquid droplet impinging onto a hot substrate, International Journal of Heat and Mass Transfer, 50 (2007) 303-319.

[41] Strotos G., Gavaises M., Theodorakakos A., Bergeles G., Numerical investigation on the evaporation of droplets depositing on heated surfaces at low Weber numbers, International Journal of Heat and Mass Transfer, 51 (2008) 1516-1529.

[42] Strotos G., Gavaises M., Theodorakakos A., Bergeles G., Numerical investigation of the cooling effectiveness of a droplet impinging on a heated surface, International Journal of Heat and Mass Transfer, 51 (2008) 4728-4742.

[43] Strotos G., Gavaises M., Theodorakakos A., Bergeles G., Evaporation of a suspended multicomponent droplet under convective conditions, in: ICHMT, Marrakech, Morocco, 2008.

[44] Strotos G., Gavaises M., Theodorakakos A., Bergeles G., Influence of species concentration on the evaporation of suspended multicomponent droplets, in: ILASS 2008, Como Lake, Italy, 2008.

[45] Nikolopoulos N., Nikas K.-S., Bergeles G., A numerical investigation of central binary collision of droplets, Computers & Fluids, 38 (2009) 1191-1202.

[46] Nikolopoulos N., Theodorakakos A., Bergeles G., Off-centre binary collision of droplets: A numerical investigation, International Journal of Heat and Mass Transfer, 52 (2009) 4160-4174.

[47] Strotos G., Nikolopoulos N., Nikas K.-S., A parametric numerical study of the head-on collision behavior of droplets, Atomization and Sprays, 20 (2010) 191-209.

[48] Theodorakakos A., Bergeles G., Simulation of sharp gas-liquid interface using VOF method and adaptive grid local refinement around the interface, International Journal for Numerical Methods in Fluids, 45 (2004) 421-439.

[49] Brackbill J.U., Kothe D.B., Zemach C., A continuum method for modeling surface tension, Journal of Computational Physics, 100 (1992) 335-354.

[50] Carslaw K.S., Jaeger J.C., Conduction of Heat in Solids, Oxford University Press, London, 1959.

[51] Incropera F.P., de Witt D.P., Fundamentals of Heat and Mass Transfer 3rd ed., Wiley, New York, 1990.

[52] Seki M., Kawamura H., Sanokawa K., Transient temperature profile of a hot wall due to an impinging liquid droplet, Journal of Heat Transfer, 100 (1978) 167-169.

[53] Qiao Y.M., Chandra S., Experiments on adding a surfactant to water drops boiling on a hot surface, Proceedings of the Royal Society of London Series a-Mathematical Physical and Engineering Sciences, 453 (1997) 673-689.

[54] Pasandideh-Fard M., Qiao Y.M., Chandra S., Mostaghimi J., Capillary effects during droplet impact on a solid surface, Physics of Fluids, 8 (1996) 650-659.

[55] Roisman I.V., Rioboo R., Tropea C., Normal impact of a liquid drop on a dry surface: model for spreading and receding, Proc. R. Soc. Lond. A 458 (2002) 1411-1430.

[56] Park H., Carr W., Zhu J., Morris J., Single Drop Impaction on a Solid Surface, AIChe J., 49 (2003) 2461-2471.

[57] Abu-Zaid M., Droplet evaporation on porous and non-porous ceramic solids heated from top, Heat and Mass Transfer, 38 (2002) 203-211.

[58] Tarozzi L., Muscio A., Tartarini P., Experimental tests of dropwise cooling on infrared-transparent media, Experimental Thermal and Fluid Science, 31 (2007) 857-865.

9 List of Tables

Table 1: Simulation parameters for the reference case (water droplet)

D_0 =	2e-3	θ_{adv} =	110^o	k_{sol} =	16.2	p =	1 bar
U_0=	1.368	θ_{rec} =	10^o	ρ_{sol} =	8030	T∞ =	293
We =	50	Pr_{liq} =	7.187	$c_{p,sol}$ =	500	T_{dr0} =	293
Re =	2649	α_{liq} =	1.44e-7	α_{sol} =	4.03e-6	T_{w0} =	373
Oh =	2.67e-3	γ_{liq} =	1583	γ_{sol} =	8065	$T_{c,th}$ =	359.88
				γ^* =	5.096	q_b'' =	470.15

Table 2: Simulation parameters for all cases examined. Blank cells denote that the missing value is equal to the one of the reference case; this is shown at the top row of the table.

case name	We	Re	Oh ($\times 10^3$)	U_0 [m/s]	D_0 [mm]	γ_{sol} [$J/m^2Ks^{0.5}$]	γ^*	T_{w0} [K]	$T_{c,th}$ [K]	q_b'' [W/m^2]
ref	50	2649	2.67	1.368	2	8065	5.10	373	359.9	470.2
We=40	40	2369		1.224						
We=60	60	2902		1.499						
D=1mm		1873	3.77	1.935	1					
D=3mm		3244	2.18	1.117	3					
T=80°C								353	343.2	327.4
T=120 °C								393	376.6	620.0
0.5γ						4057	2.56		350.6	
2.0γ						16130	10.2		365.9	

10 List of Figures

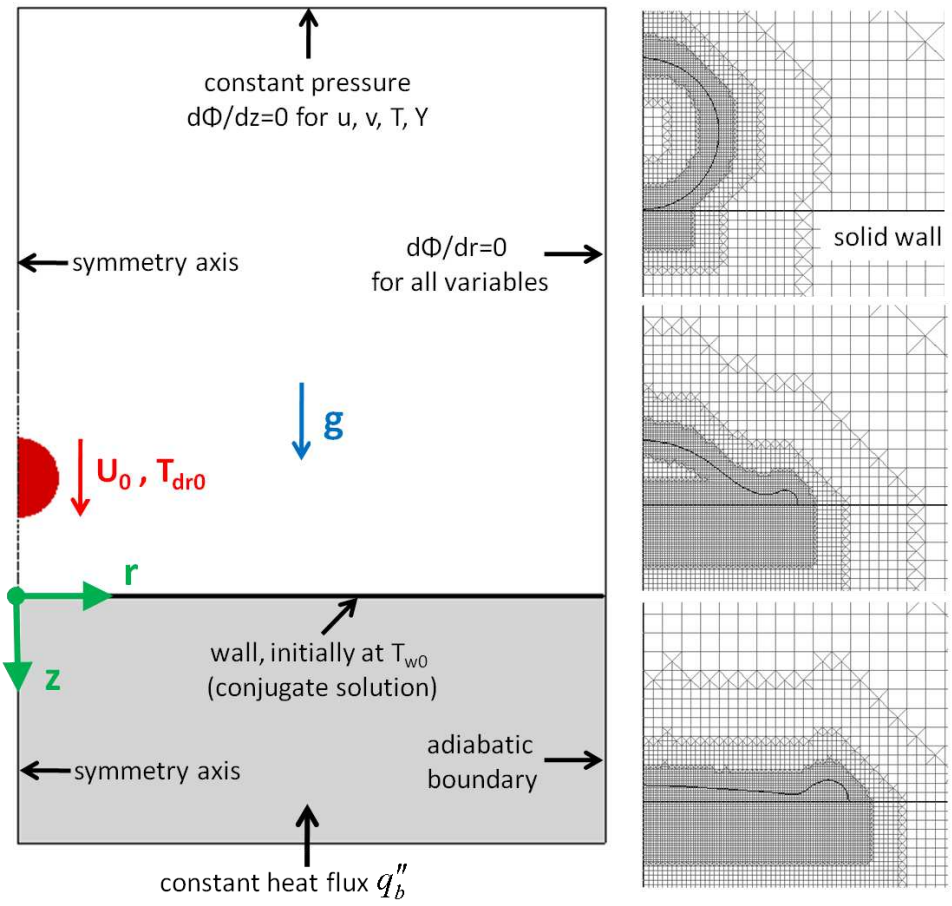

Fig. 1: The computational domain together with the boundary conditions used is shown on the left-hand-side. On the right-hand-side, a detail of the dynamical locally refined grid is shown, both for the fluid and solid regions, using four levels of local refinement.

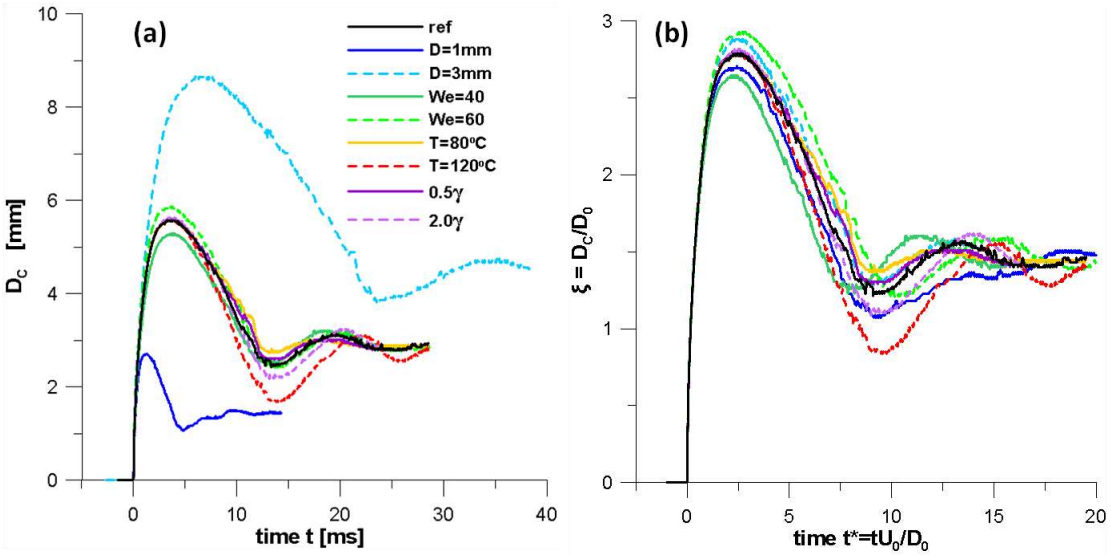

Fig. 2: Temporal evolution of the droplet spreading in (a) dimensional and (b) and non-dimensional units.

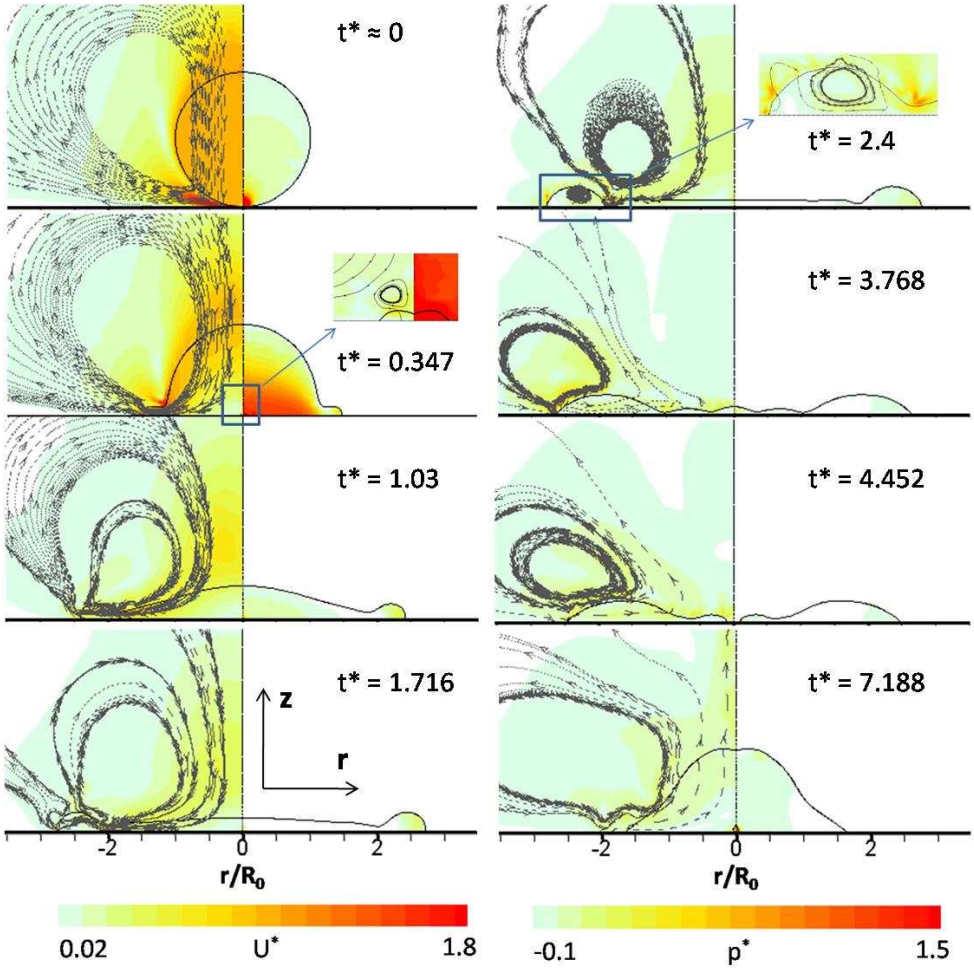

Fig. 3: Temporal evolution of the non-dimensional velocity field (left-hand-side of pictures) and non-dimensional pressure field (right-hand-side of pictures) for the reference case.

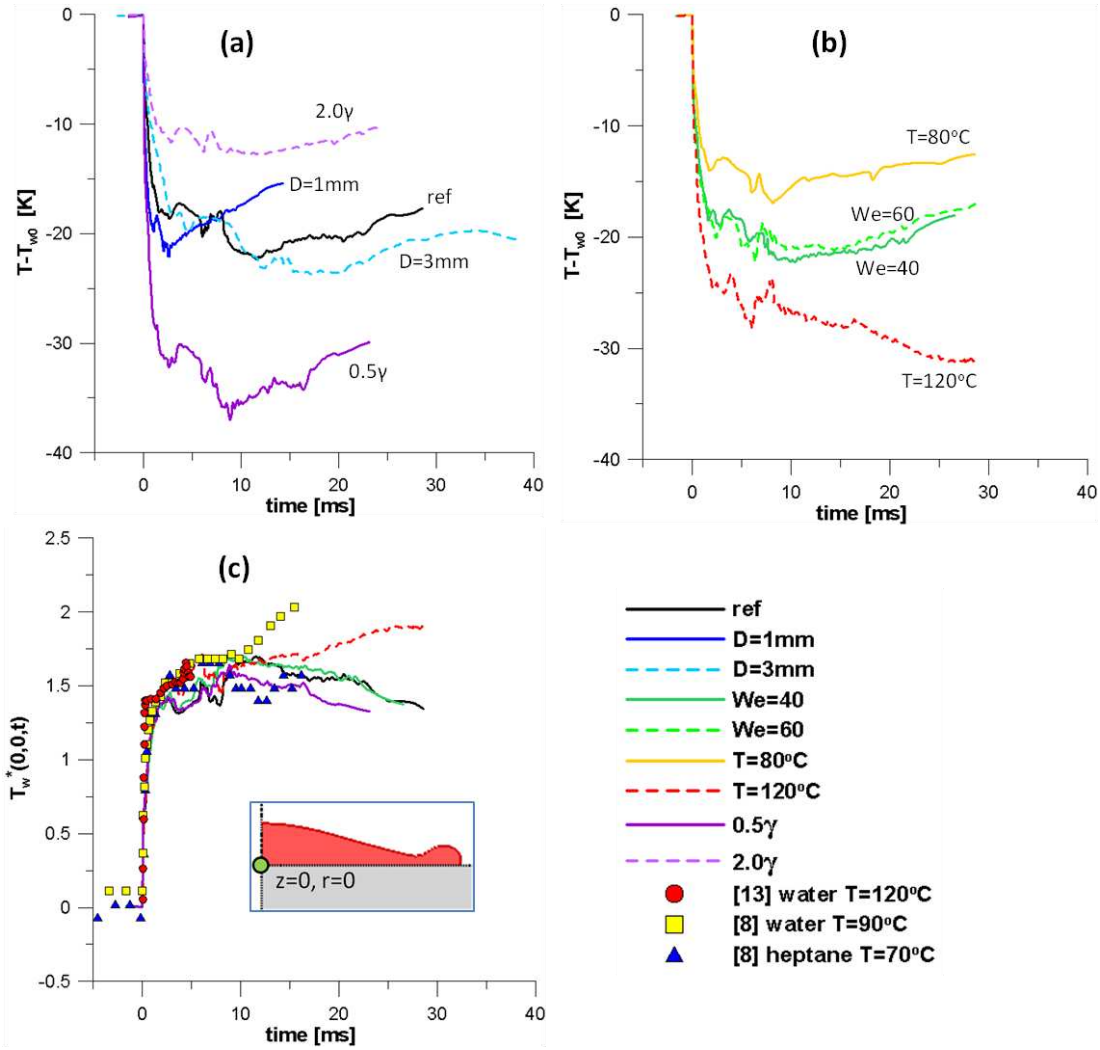

Fig. 4: Temporal evolution of the cooling of the substrate in (a,b) dimensional units and (c) non-dimensionalised. The inset figure in (c) shows the point examined (z=0, r=0).

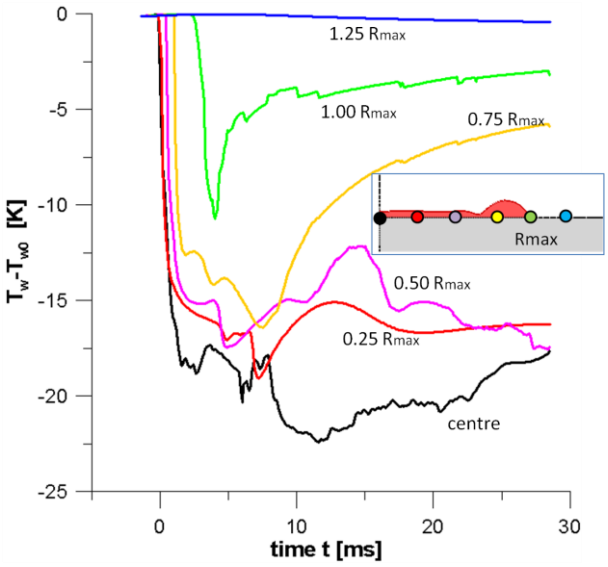

Fig. 5: Temporal evolution of the temperature of the upper solid surface (z=0) at various distances from the axis of symmetry for the reference case. The inset figure shows the points examined.

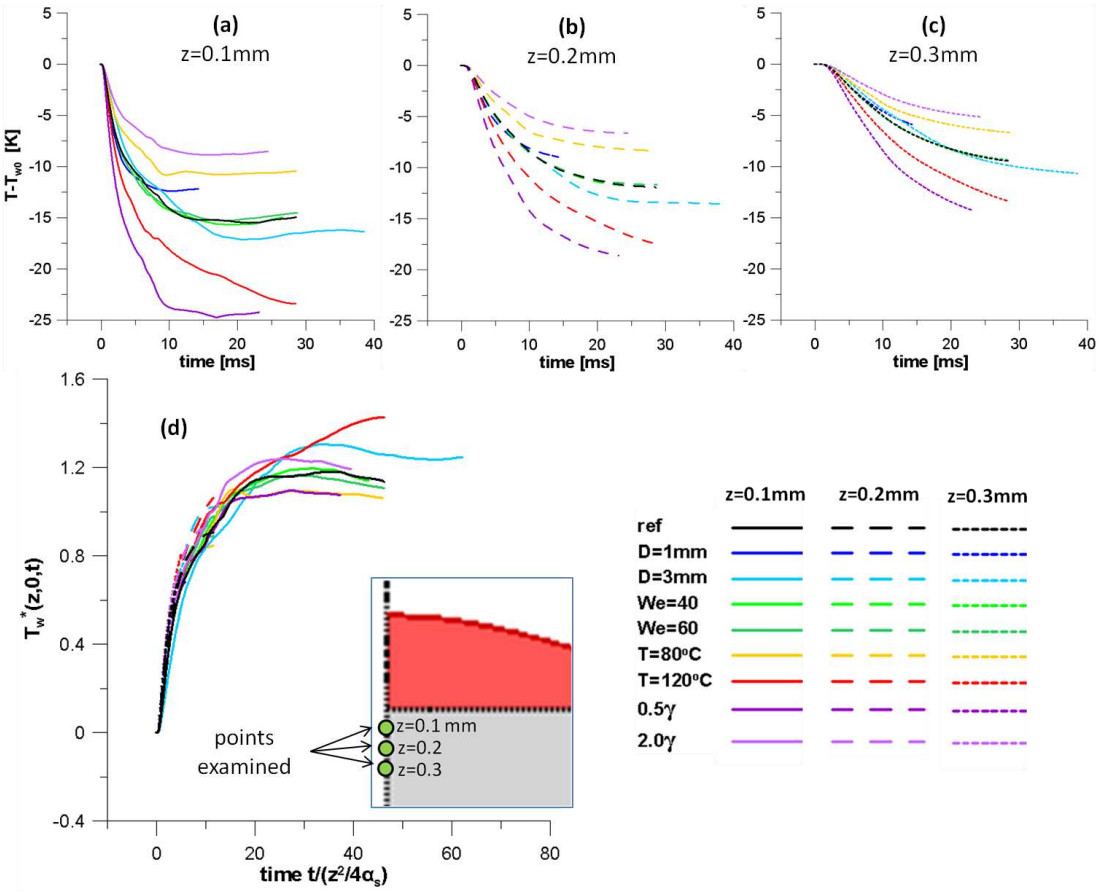

Fig. 6: Temporal evolution of the cooling of the substrate at symmetry axis (r=0) at three distances from the upper surface in dimensional units (a, b, c) and non-dimensionalised (d). The inset figure shows the points examined.

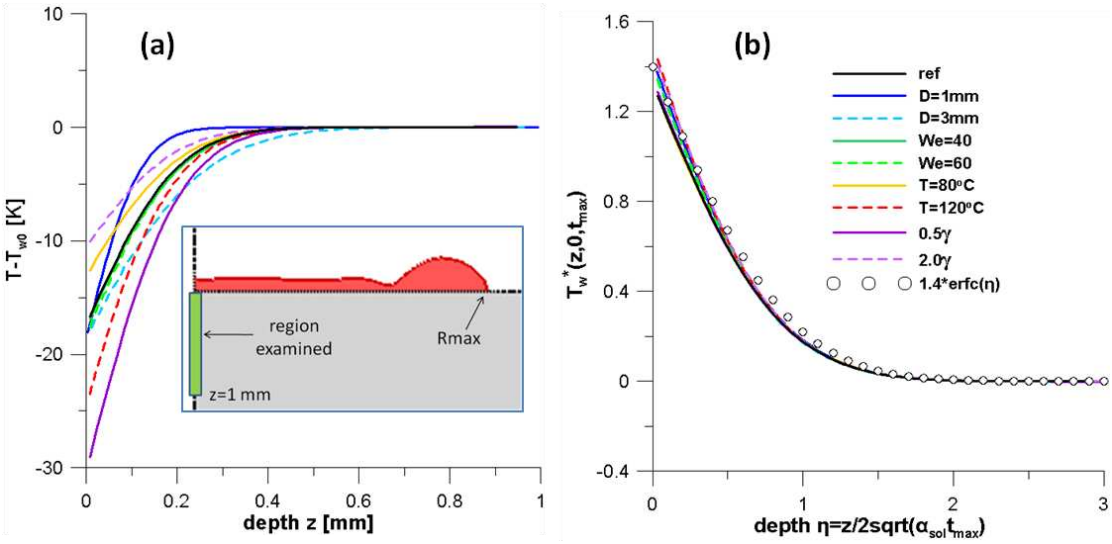

Fig. 7: Temperature distribution at maximum spreading of the solid wall along the symmetry axis (r=0) for all cases examined (a) in dimensional units and (b) non-dimensionalised. The inset figure shows the region examined.

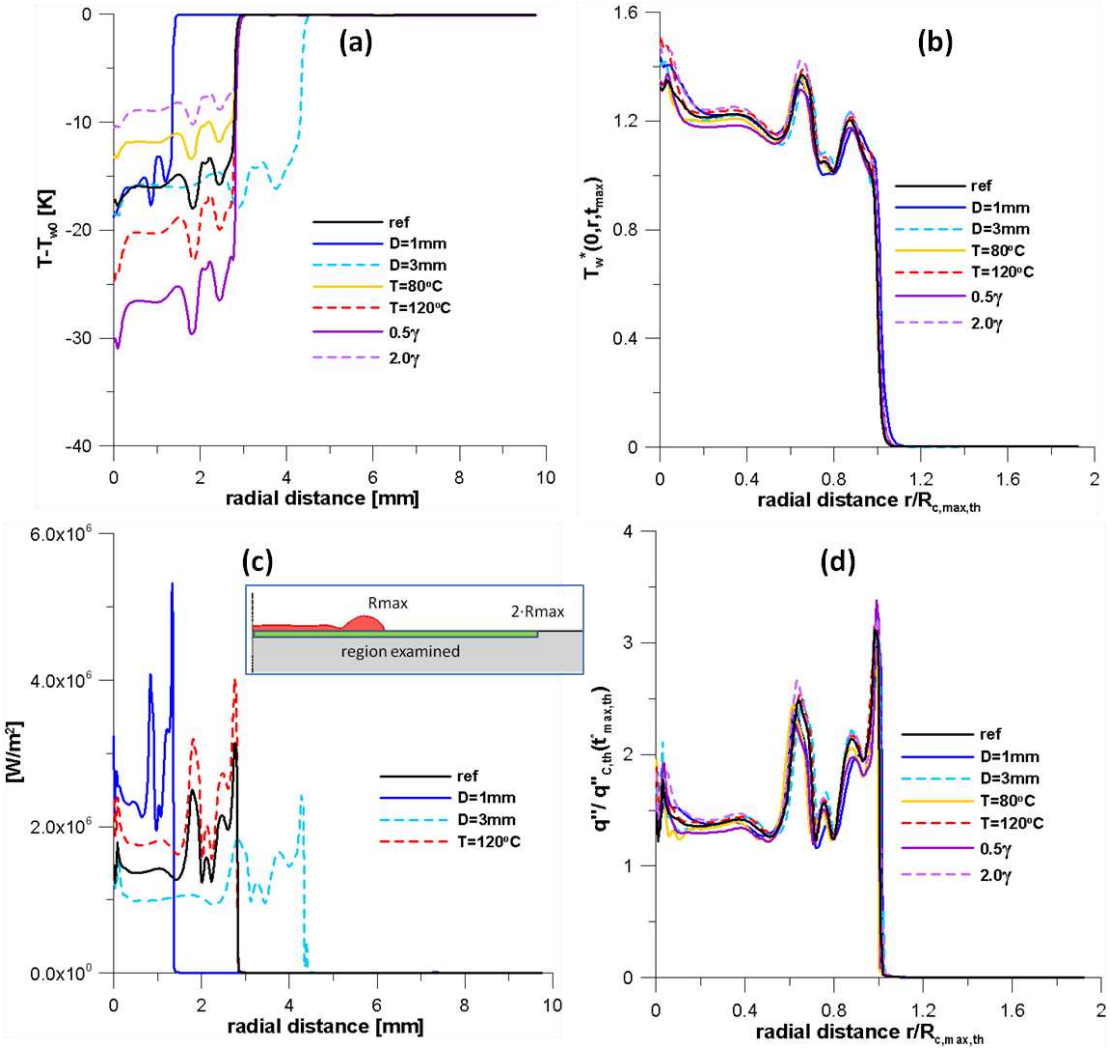

Fig. 8: (a) Temperature distribution of the solid wall in the radial coordinate in dimensional units and (b) non-dimensionalized, (c) heat flux distribution of the solid wall in the radial coordinate in dimensional units and (d) non-dimensionalized. The plots presented refer to the time of maximum spreading at the upper solid surface (z=0), while the inset figure shows the region examined.

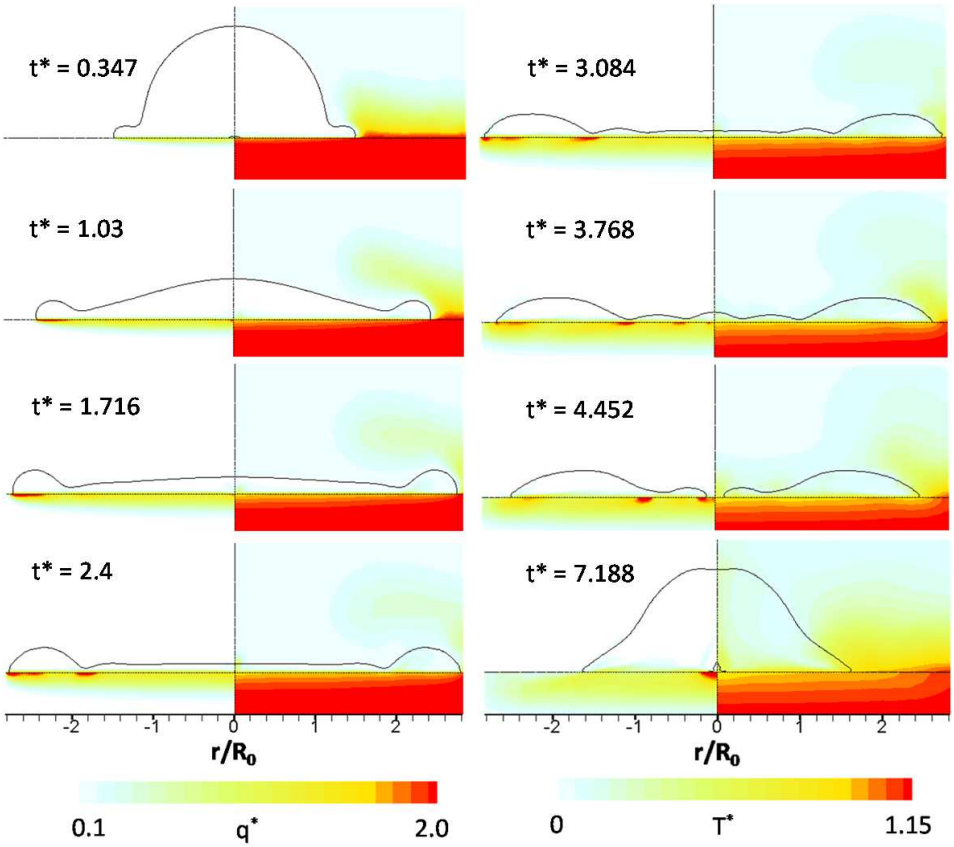

Fig. 9: Temporal evolution of non-dimensional heat flux field (left-hand-side of pictures) and non-dimensional temperature field (right-hand-side of pictures) for the reference case.

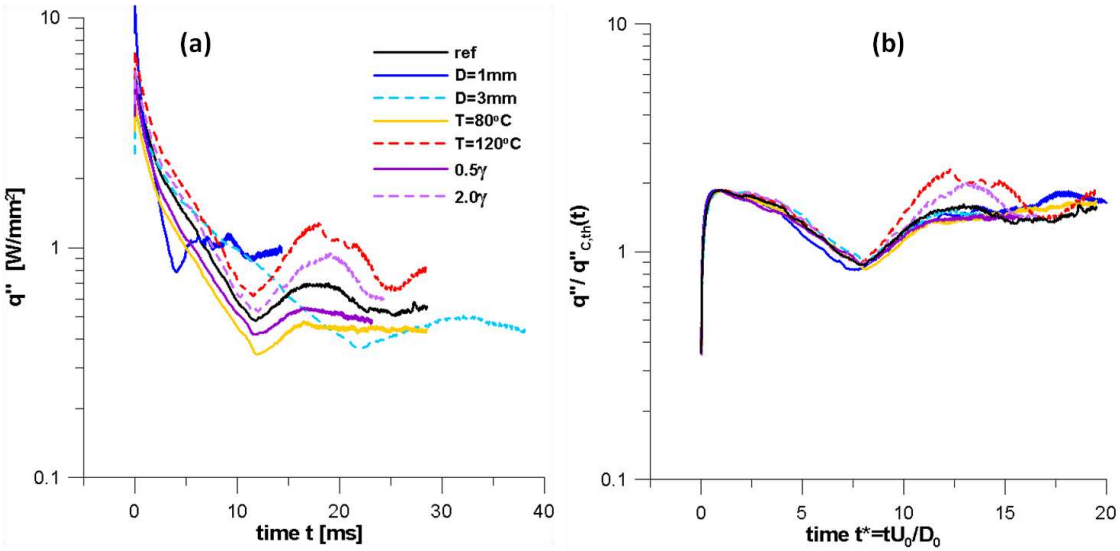

Fig. 10: Temporal evolution of (a) the mean heat flux absorbed from the droplet in dimensional units and (b) non-dimensionalised using the transient conduction theory.

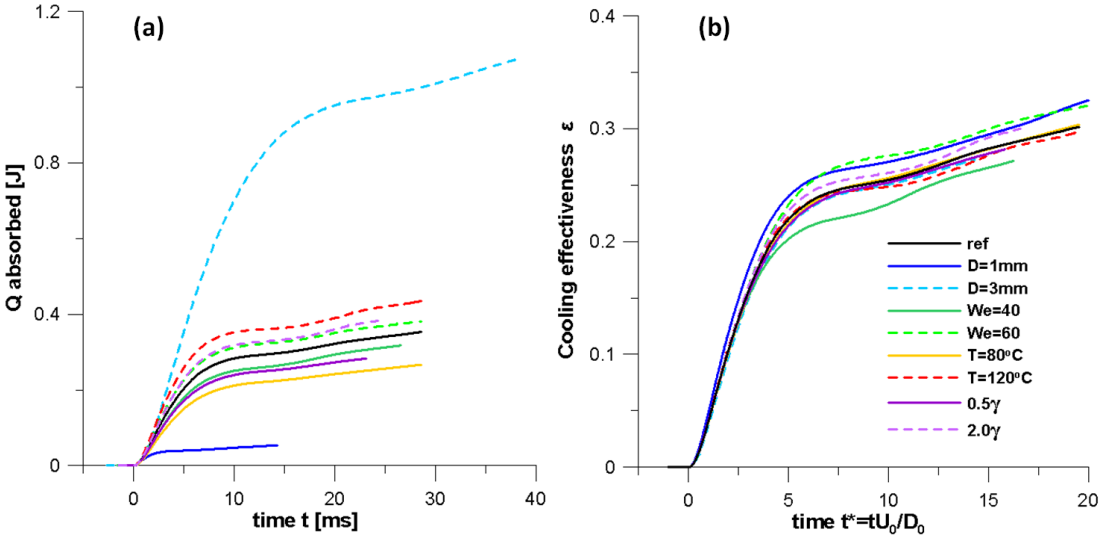

Fig. 11: Temporal evolution of (a) the total energy absorbed by the droplet in dimensional units and (b) non-dimensionalised representing the cooling effectiveness.

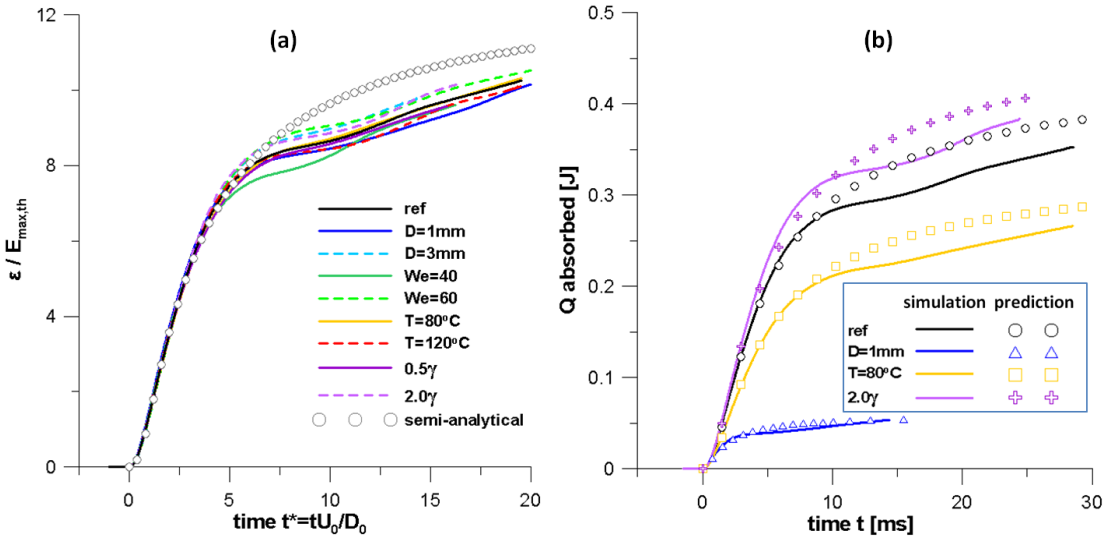

Fig. 12: (a) Normalized cooling effectiveness plotted along with the semi-analytical expression, (b) temporal evolution of the total energy absorbed by the droplet for selected cases. In (b) the solid lines correspond to VOF predictions and the symbols to the corresponding predictions with the semi-analytical expression.

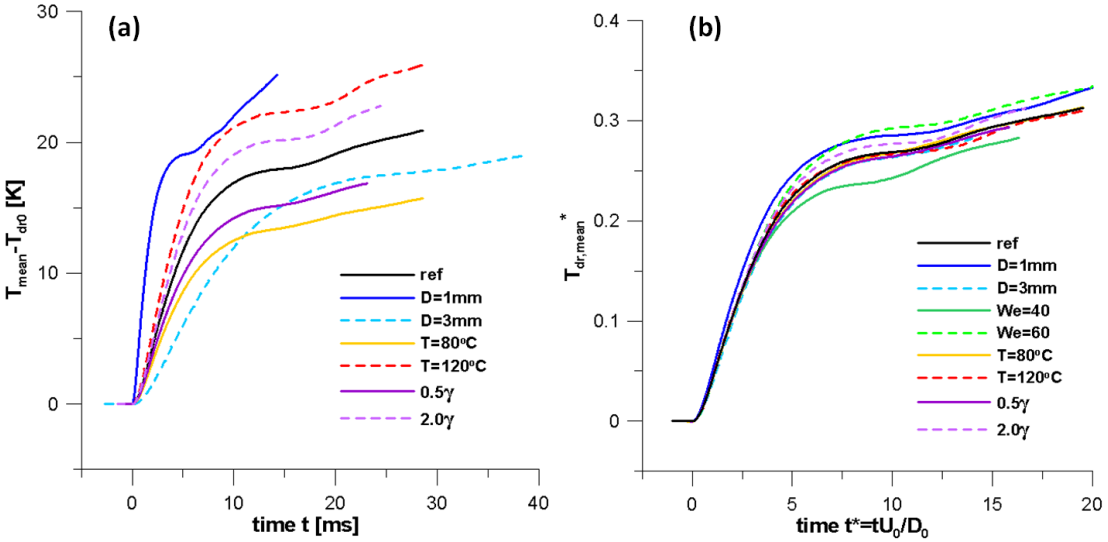

Fig. 13: Temporal evolution of the mean volume-averaged droplet temperature in (a) dimensional units and (b) non-dimensionalised.

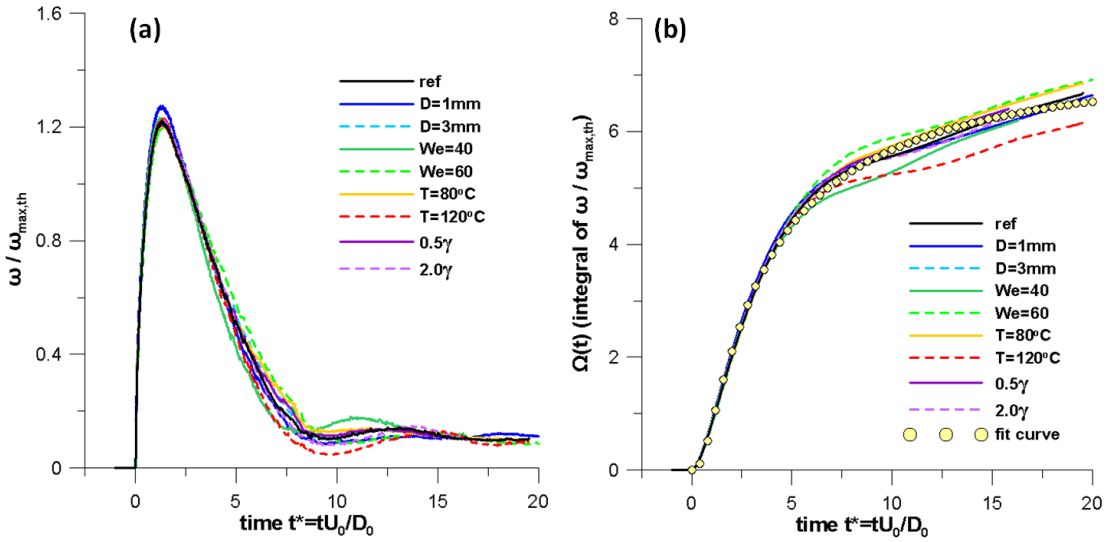

Fig. 14: Temporal evolution of (a) term $\omega/\omega_{max,th}$ and (b) its integral Ω along with the best fit curve.